Sparse Recovery Methods Hold Promise for Diffuse Optical Tomographic Image Reconstruction

Jaya Prakash, Calvin B. Shaw, Rakesh Manjappa, Rajan Kanhirodan, and Phaneendra K. Yalavarthy

***Abstract*—The sparse recovery methods utilize the ℓ_p-norm-based regularization in the estimation problem with $0 \leq p \leq 1$. These methods have a better utility when the number of independent measurements are limited in nature, which is a typical case for diffuse optical tomographic image reconstruction problem. These sparse recovery methods, along with an approximation to utilize the ℓ_0-norm, have been deployed for the reconstruction of diffuse optical images. Their performance was compared systematically using both numerical and gelatin phantom cases to show that these methods hold promise in improving the reconstructed image quality.**

***Index Terms*—Near infrared imaging, diffuse optical tomography, image reconstruction, sparse recovery methods.**

I. Introduction

NEAR infrared diffuse optical tomography is an emerging biomedical imaging modality that uses wavelength in the range of 600–1000 nm with a capability to provide functional information of the tissue under investigation [1]–[3]. The main imaging applications include breast cancer imaging and brain function assays [4]–[7]. The near infrared (NIR) light is delivered and collected at the boundary using fibre bundles, these boundary measurements are in turn used to reconstruct the internal tissue optical properties like absorption and scattering coefficients [3]. The reconstructed optical images suffer from the lack of sharp features, mainly due to the diffusive nature of NIR light, arising from multiple scattering of photons [6], [7].

The reconstruction of optical properties in diffuse optical tomography is ill-posed due to dominance of scattering as well as limited available boundary data [7], [8]. To obtain unique solution, typically a regularization scheme is included in the image reconstruction procedure [9]. The well-established Tikhonov type regularization (quadratic penalty, ℓ_2-norm) imposes a smoothness constrain, leading to suppression of noise and discouraging sharp edges in the reconstructed image [10].

Recently sparse recovery methods have been proposed to show that ℓ_1-norm and ℓ_p-norm-based regularization methods impose a sparsity constrain, facilitating the recovery of sharp edges and being robust with noise in time-domain diffuse optical tomography [11]. Most methods in the literature do not deal with sparsity constraint, which relates the minimum number of required measurements to the sparsity of the image (or vice versa), which can provide insight into the deployment of these sparse recovery methods (ℓ_1-norm and ℓ_p-norm) for diffuse optical image reconstruction problem. More importantly, the application of ℓ_0-norm (or its approximation)-based regularization has not been proposed for diffuse optical tomographic image reconstruction, which is known to provide a high level of sparsity induced solutions. The application of ℓ_0-norm-based sparse recovery methods is inspired by the recent progress reported in the signal processing community [12], typically applied in low-noisy environments.

This study aims to show that sparse recovery methods, all ℓ_p-norm-based regularization with $0 \leq p \leq 1$, hold promise in diffuse optical tomographic image reconstruction with a special emphasis on ℓ_0-norm-based regularization. Note that the ℓ_0-norm is approximated by smooth version of ℓ_0-norm [12]. For completeness, the comparison also includes the traditional ℓ_2-norm (Tikhonov)-based regularization scheme. The effectiveness of the sparse recovery methods is shown using both numerical and gelatin phantom cases, where the number of measurements were fixed and sparsity in the target (or expected) images is varied. Moreover, a case of varying noise level is also taken up to test the robustness level of these sparse recovery methods to the data noise. Note that in this study sparsifying transformation, which can make any image as a sparse one, is not performed in the reconstruction scheme to avoid the bias introduced by these transforms with also keeping in mind most tumors tend to be highly localized, making the original reconstruction problem itself as a sparse one. The discussion in this study is limited to a 2-D continuous wave (CW) case as the emphasis is on bringing out the promise of sparse recovery methods for diffuse optical tomography.

II. Methods

A. Diffuse Optical Tomography—Forward Problem

The diffuse optical image reconstruction problem, also known as inverse problem, is a model-based iterative scheme, which

Manuscript received May 31, 2013; revised August 6, 2013; accepted August 6, 2013. J. Prakash and C. B. Shaw equally contributed. This work was supported in part by the Department of Atomic Energy, Government of India through DAE young scientist research award (Sanction No. 2010/20/34/6/BRNS) and in part by the Department of Biotechnology (DBT) Rapid Grant for Young investigators (RGYI) (No: BT/PR6494/GDB/27/415/2012). The work of J. Prakash was supported by Microsoft Corporation and Microsoft Research India under the Microsoft Research India Ph.D. Fellowship Award and SPIE Optics and Photonics Education Scholarship.

J. Prakash, C. B. Shaw, and P. K. Yalavarthy are with the Supercomputer Education and Research Centre, Indian Institute of Science, Bengaluru 560012, India (e-mail: jayaprakash@ssl.serc.iisc.in; calvin@ssl.serc.iisc.in; phani@serc.iisc.in).

R. Manjappa and R. Kanhirodan are with the Department of Physics, Indian Institute of Science, Bengaluru 560012, India (e-mail: rakesh@physics.iisc.ernet.in; rajan@physics.iisc.ernet.in).

Color versions of one or more of the figures in this paper are available online at http://ieeexplore.ieee.org.

Digital Object Identifier 10.1109/JSTQE.2013.2278218

uses repeatedly the computational model of light propagation in tissue (forward problem). This computational model deploys diffusion equation (DE), which is known to be a reasonable approximation to radiative transfer equation (RTE), in case of thick tissues (such as breast and brain). In a CW-case, the DE is given by [13]

$$-\nabla.\,[D(r)\nabla\Phi(r)] + \mu_a(r)\Phi(r) = Q_o(r) \tag{1}$$

where $\Phi(r)$ is the photon density (real values) at position r and $Q_o(r)$ represents the isotropic light source. The optical absorption coefficient is represented by $\mu_a(r)$ and the optical diffusion coefficient ($D(r)$) is defined as

$$D(r) = \frac{1}{3[\mu_a(r) + \mu_s'(r)]} \tag{2}$$

where $\mu_s'(r)$ represents the reduced scattering coefficient, assumed to be known in CW case. Robin (type-III) boundary condition is used to model the refractive-index mismatch at the tissue boundary [14]. The fluence ($\Phi(r)$) is sampled at the measurement position to obtain the modeled data, i.e., $G(\mu_a) = S\{\Phi(r)\} = S\{F(\mu_a)\}$, where S is the sampling matrix (containing source/detector positions) and F is the forward computational model which is used to compute the fluence [9]. Here, F represents the finite-element method, which gives immense flexibility in terms of numerical modeling of irregular geometries, such as breast and brain [7], [8], [13]. The experimentally obtained CW data are represented by $y\,(= \ln(A)$, with A being amplitude of the data). For the CW case, it is assumed that $\mu_s'(r)$ to be a known constant, making the unknown (or parameter to be estimated) as $\mu_a(r)$.

B. Diffuse Optical Tomographic Image Reconstruction

The image reconstruction (or inverse problem) procedure involves matching the experimental data (y) with the modeled data ($G(\mu_a)$) in a least-squares sense [9]. As this problem is ill-posed, typically a regularization term is added to bring stability and uniqueness to the estimation process.

1) Tikohonov Minimization Scheme (ℓ_2-Norm Based Regularization): The most popular regularization scheme is the Tikohonov minimization scheme, that deploys ℓ_2-norm of the unknown parameter. The objective (or cost) function in this case turns out to be

$$\Omega(\mu_a) = \|y - G(\mu_a)\|_2^2 + \lambda\|\mu_a\|_2^2. \tag{3}$$

The regularization parameter is given by λ and $\|.\|_2^2$ represents the square of the ℓ_2-norm. The function $G(\mu_a)$ can be expanded using a Taylor series expansion around μ_{a0} as

$$G(\mu_a) = G(\mu_{a0}) + \mathbf{J}\triangle\mu_a + (\triangle\mu_a)^T\mathbf{S}\triangle\mu_a + \cdots \tag{4}$$

with $\mathbf{J} = \frac{\partial G(\mu_a)}{\partial \mu_a}$ representing the Jacobian [dimension: $M \times N$, with M representing the number of measurements and N representing the number of FEM nodes (unknowns)] and $\mathbf{S}$ represents the Hessian (second-order derivative). $\triangle\mu_a$ is the update given as $\mu_a - \mu_{a0}$. Linearizing the previous equation leads to an objective function [15]

$$\Omega(\triangle\mu_a) = \|\delta - \mathbf{J}\triangle\mu_a\|_2^2 + \lambda\|\triangle\mu_a\|_2^2 \tag{5}$$

with $\delta = y - G(\mu_a)$ being the data-model misfit. The Gauss—Newton update equation that results by minimizing the aforementioned objective function is [16]

$$(\mathbf{J}^T\mathbf{J} + \lambda\mathbf{I})\triangle\mu_a = \mathbf{J}^T\delta. \tag{6}$$

The Jacobian is typically computed using the adjoint method [13], where the forward problem is solved twice, one for the regular source term and another for adjoint source. The update equation provides a direct estimation of $\triangle\mu_a$, after computation, it is added to the current μ_a, resulting in a new estimate of μ_a. Using this μ_a, both $G(\mu_a)$ and $\mathbf{J}$ are recomputed for getting new update using (6). This process is repeated until the difference in $\|\delta\|_2^2$ in subsequent iterations becomes lesser than 2%.

This ℓ_2-norm-based method has been widely used for estimation of the optical properties in diffuse optical tomographic image reconstruction. Due to ℓ_2-norm of the parameters, the objective function is a convex function, which has a clear minima. At the same time, this norm only allows smooth solutions for the problem at hand, discouraging the sharp features in the reconstructed images. Moreover, this assumes that the parameter function is smooth piece-wise continuous function (allowing twice differentiability), encouraging dense solutions (sparseness being absent).

As most tumors are known to be highly localized, it is a good approximation to assume that the reconstructed μ_a is going to be sparse, especially in cases where one knows the background μ_a of the imaging domain. This background μ_a (constant value throughout the domain) could be easily estimated using any of the data calibration procedures that approximates the imaging domain as semiinfinite [17]. The sparse recovery methods, where the ℓ_p-norm is used in the regularization with $0 \leq p \leq 1$, known to provide sparse solutions (with $p = 0$ encouraging highest sparsity in the solution) as well as sharp changes in the recovered μ_a distribution.

2) Sparse Recovery Method (ℓ_p-Norm Based With $0 < p \leq 1$): The unconstrained objective function to be minimized with respect to $\triangle\mu_a$ in this case can be written as

$$\Omega'(\triangle\mu_a) = \|\delta - \mathbf{J}\triangle\mu_a\|_2^2 + \lambda\|\triangle\mu_a\|_p^p \tag{7}$$

with $p = 2$, it reverts to (5). The aforementioned cost function becomes a nonconvex one, when $0 < p < 1$, which can not be solved directly. In order to overcome this limitation, we adopt a homotopy-like cooling approach with a help of majorization–minimization (MM) framework as proposed in Refs. [18]–[21]. The MM replaces the objective function to be solved by a sequence of simpler minimization problems. The function $\Omega'(\triangle\mu_a)$ is minimized starting off with an initial guess $\triangle\mu_a^k$ and a new vector, $\triangle\mu_a^{(k+1)}$ is found which further decreases $\Omega'(\triangle\mu_a)$; in summary the following relation needs to be satisfied

$$\Omega'(\triangle\mu_a^{(k+1)}) < \Omega'(\triangle\mu_a^k). \tag{8}$$

The aforementioned condition is met using a new function $H(\triangle\mu_a)$ which majorizes $\Omega'(\triangle\mu_a)$ and the new function is minimized to get the new update ($\triangle\mu_a^{(k+1)}$). In addition the new function ($H(\triangle\mu_a)$) should be chosen such that $H(\triangle\mu_a) \geq$

$\Omega'(\triangle\mu_a)$ for all $\triangle\mu_a$ and $H(\triangle\mu_a)$ should equal $\Omega'(\triangle\mu_a)$ at $\triangle\mu_a^k$.

In order to minimize $\Omega'(\triangle\mu_a)$, initially the data-fidelity term ($\|\delta - \mathbf{J}\triangle\mu_a\|$) of (7) is considered.

$$\Omega_1(\triangle\mu_a) = \|\delta - \mathbf{J}\triangle\mu_a\|_2^2. \tag{9}$$

For this minimization, the new function, $H_k(\triangle\mu_a)$ is chosen to be

$$H_k(\triangle\mu_a) = \|\delta - \mathbf{J}\triangle\mu_a\|_2^2 + (\triangle\mu_a - \triangle\mu_a^k)^T(\alpha\mathbf{I} - \mathbf{J}\mathbf{J}^\mathbf{T})(\triangle\mu_a - \triangle\mu_a^k). \tag{10}$$

In here, α is the maximum eigen value of the matrix $\mathbf{J}^\mathbf{T}\mathbf{J}$ and $\mathbf{I}$ is the identity matrix. Minimizing the previous function is same as minimizing the following function:

$$H_k(\triangle\mu_a) = \|b - \triangle\mu_a\|_2^2 \tag{11}$$

where $b = \triangle\mu_a^k + \alpha^{-1}(\mathbf{J}^\mathbf{T}(\delta - \mathbf{J}\triangle\mu_a^k))$. Note that this update is known as the Landweber iteration. The second step in MM framework is to include the regularization term ($\lambda\|\triangle\mu_a\|_p^p$) in the function $H_k(\triangle\mu_a)$, this results in the following cost function:

$$H_k'(\triangle\mu_a) = \|b - \triangle\mu_a\|_2^2 + \frac{\lambda}{\alpha}\|\triangle\mu_a\|_p^p. \tag{12}$$

Now, the previous function is minimized by using the first-order condition, which requires computing the partial derivatives of the function given by

$$\frac{\partial H_k'(\triangle\mu_a)}{\partial\triangle\mu_a(i)} = 2b(i) - 2\triangle\mu_a(i) + \frac{\lambda}{\alpha}p|\triangle\mu_a(i)|^{p-1}\text{sgn}(\triangle\mu_a(i)) \tag{13}$$

where sgn($\triangle\mu_a(i)$) is the *signum* function defined as

$$\text{sgn}(\triangle\mu_a(i)) = \begin{cases} 1 & \text{for } \triangle\mu_a(i) > 0, \\ -1 & \text{for } \triangle\mu_a(i) < 0, \\ 0 & \text{for } \triangle\mu_a(i) = 0. \end{cases} \tag{14}$$

Now, setting the partial derivatives to zero and solving for $\triangle\mu_a(i)$, the following update equation is obtained

$$\triangle\mu_a(i) = \text{sgn}(b(i))\max\left(0, |b(i)| - p\frac{\lambda}{2\alpha}|b(i)|^{p-2}\right). \tag{15}$$

Hence, the MM-framework for minimizing the objective function in (7) can be summarized using a two-step iterative solution [18] as given in Fig. 1. In this study, Algorithm 1 was used for all cases $0 < p \leq 2$ for fair comparison of the results.

For $p = 0$, the smooth-ℓ_0 framework is used to solve the objective function, which will be introduced in the following section. The inputs to Algorithm 1 consist of certain specifications such as d and Tol, where d is required to iteratively reduce (cool) the value of λ and the value of *Tol* is used as terminating condition for the inner loop based on the relative change of the cost function. The values of α and λ correspond to the step size and the initial regularization parameter. The value of α was set to one in all cases, but λ was chosen empirically in each case for faster convergence.

Till now the regularization terms contain the norms of unknowns with $0 < p \leq 2$, where the sparsity in the expected

INPUT: y, μ_{a0} (initial guess), λ, d (decrease factor for cooling λ), p, in_{it}
OUTPUT: μ_a
Initialize: m1 = m2 = 0; it = 1, σ = 1e-5, Tol = 1e-6, $\alpha = 1$, $\triangle\mu_a^0 = 0$ (zero vector).
1. Compute $\mathbf{J}$ and $G(\mu_a)$
2. Estimate $\delta_{it} = y - G(\mu_a)$; m2 = $||\delta_{it}||_2{}^2$

if $(\frac{m2-m1}{m2}) * 100 > 2$
$i = 1$
Outer Loop: While $||\delta_{it} - \mathbf{J}\triangle\mu_a^k||_2^2 > \sigma$ or $i < in_{it}$.
  Initialize: $\Omega_k = 1e2 + 1$, $\Omega_{k+1} = 1e2$.
  While $\frac{\Omega_k - \Omega_{k+1}}{\Omega_k + \Omega_{k+1}} \geq$ Tol
    a. set $\Omega_k = \Omega_{k+1}$.
    b. b=$\triangle\mu_a^k + \alpha^{-1}\mathbf{J}^\mathbf{T}(\delta_{it} - \mathbf{J}\triangle\mu_a^k)$
    c. $\triangle\mu_a^k$ =*sgn*(b)*max*(0, $|b| - p\frac{\lambda}{2\alpha}$*diag*($|b|^{p-2}$))
    d. Compute $\Omega_{k+1} = ||\delta_{it} - \mathbf{J}\triangle\mu_a^k||_2^2 + \lambda||\triangle\mu_a^k||_p^p$.
  End While
3. $\lambda = d \times \lambda$; $i = i + 1$.
Outer Loop: End While
4. $\mu_a = \mu_a + \triangle\mu_a^k$.
5. m1 = m2; it = it +1; go to step-1.

else
  Return μ_a (output)
end

Fig. 1. Algorithm 1. Based ($0 < p \leq 2$) sparse recovery algorithm.

solution is inversely proportional to the p value. Specifically, the sparsest solution can be found when $p = 0$. But the problem of using exact ℓ_0-norm, which mainly counts the nonzero elements (counts the cardinality), is an NP-hard problem [22]. Typically, one employs an approximation to the ℓ_0-norm to get around this problem, one such approximation is smooth-ℓ_0-norm.

3) Sparse Estimation Using Smooth-ℓ_0 Norm: The objective function in this case can be written as

$$\tilde{\Omega}(\triangle\mu_a) = \|\delta - J\triangle\mu_a\|_2^2 + \lambda\|\triangle\mu_a\|_0. \tag{16}$$

In this study, the ℓ_0-norm is minimized using a well-established smooth-ℓ_0 scheme [12], [23], [24]. The smooth-ℓ_0-norm was approximated with the help of Gaussian function, which is given by

$$\rho(\triangle\mu_a) = e^{\frac{-\triangle\mu_a^2}{\sigma^2}}. \tag{17}$$

It can be clearly seen that as $\triangle\mu_a$ tends to 0, $\rho(\triangle\mu_a)$ will tend to 1. On the other hand if σ tends to 0, $\rho(\triangle\mu_a)$ will tend to 0. In other words, the mathematical definition of $\rho(\triangle\mu_a)$ becomes [12]

$$\rho(\triangle\mu_a) = \begin{cases} 1 & \text{if } |\triangle\mu_a| \ll \sigma, \\ 0 & \text{if } |\triangle\mu_a| \gg \sigma. \end{cases} \tag{18}$$

Hence, the ℓ_0-norm can be written as

$$\|\triangle\mu_a\|_0 = N - \sum_{i=1}^{N}\rho(\triangle\mu_{a_i}). \tag{19}$$

The maximization of function given by (18) will be same as minimization of function given by (19).

INPUT: y, μ_{a0} (initial guess), λ, σ_{dec} (decreasing factor), μ_0 (step-size)
OUTPUT: μ_a
Initialize: m1 = m2 = 0; it = 1, $\sigma_{min} = 10^{-9}$, $iter$ = 3;

1. Compute $\mathbf{J}$ and $G(\mu_a)$
2. Estimate $\delta_{it} = y - G(\mu_a)$; m2 = $||\delta_{it}||_2{}^2$

if $(\frac{m2-m1}{m2}) * 100 > 2$

3. $\mathbf{J}_{pseudo} = (\mathbf{J}^T\mathbf{J} + \lambda\mathbf{I})^{-1}\mathbf{J}^T$ and $\triangle\mu_a = \mathbf{J}_{pseudo}\delta_{it}$.
4. σ_{it} = 2*$max(|(\triangle\mu_a)|)$

`while` $\sigma_{it} \geq \sigma_{min}$
for i=1 to $iter$

6. $\triangle_{Gauss} = \triangle\mu_a e^{\frac{-|(\triangle\mu_a)|^2}{\sigma_{it}^2}}$
7. $\triangle\mu_a = \triangle\mu_a - \mu_0\triangle_{Gauss}$
8. $\triangle\mu_a = \triangle\mu_a - \mathbf{J}_{pseudo}(\mathbf{J}\triangle\mu_a - \delta_{it})$

end

9. $\sigma_{it} = \sigma_{it}\sigma_{dec}$.

`end`

10. $\mu_a = \mu_a + \triangle\mu_a$.
11. m1 = m2; it = it +1; go to step-1.

else

Return μ_a (output)

end

Fig. 2. Algorithm 2. Smooth-ℓ_0-norm based sparse recovery algorithm.

The method of Lagrange multipliers is used for maximizing (18) subject to $J\triangle\mu_a = \delta$, leading to the objective function [12]

$$\tilde{\Omega}(\triangle\mu_a) = \sum_{i=1}^{N} \rho(\triangle\mu_{a_i}) - \tilde{\lambda}^T(J\triangle\mu_a - \delta). \tag{20}$$

The partial derivative of the previous equation is evaluated with respect to $\triangle\mu_a$ resulting in a Karush–Kuhn–Tucker (KKT) conditions to solve for *N*+*M* unknowns (*N* of $\triangle\mu_a$ and *M* of $\tilde{\lambda}$). The linear system to be solved now is [12]

$$\begin{cases} \left[\triangle\mu_{a1}e^{\frac{-\triangle\mu_{a1}^2}{\sigma^2}} \ldots \triangle\mu_{aNN}e^{\frac{-\triangle\mu_{aNN}^2}{\sigma^2}}\right] - J^T\lambda_1 = 0 \\ J\triangle\mu_a - \delta = 0 \end{cases} \tag{21}$$

where λ_1 is $-\sigma^2\tilde{\lambda}$. In other words, it can be clearly seen that the function defined in (18) is a dual for ℓ_0-norm when the σ tends to a very small value ($\sigma \leq \triangle\mu_a$).

The Smooth-ℓ_0 norm method tries to maximize (17) using a steepest ascent Algorithm, will in turn minimize the $\|\triangle\mu_a\|_0$ of the function. The overall non-linear image reconstruction Algorithm using the Smooth-ℓ_0 norm method is given in Algorithm 2. It was shown in [12] that (21) will be an update to the ℓ_2-norm-based method as σ takes a very high value.

The value of $\sigma_{\min}$ is 10^{-9} is chosen to approximate the ℓ_0-norm, specifically the lowest value of the norm [12]. The step 7 in Algorithm 2 (see Fig. 2) indicates the steepest ascent step which maximizes the derivative of the Gaussian function defined in step 6 ($\triangle_{\mathrm{Gauss}}$). It can be observed that the steepest ascent Algorithm is repeated only for 3 iterations (iter = 3), ensuring the faster convergence, running for each σ_{it} defined by a decreasing sequence [12]. The step 8 indicates the projection taken on to the convex set, this step is performed to avoid trapping of the steepest ascent Algorithm in a local maxima [12]. The steepest ascent Algorithm uses a decreasing variance step (step 9 of Algorithm 2) with σ_{dec} dictating the decreasing sequence and taking a value between 0 and 1. Another important observation is that if $\sigma_{\min}$ is chosen to have a high value (close to 1), then the obtained solution will lead to an ℓ_2-norm-based solution [12]. The μ_0 in the Algorithm 2 (step-7) is a positive constant that acts as a step size for the steepest ascent method.

In compressive sensing, it is well known that, if one uses Z incoherent (independent) measurements, the number of parameters that could be exactly reconstructed (represented by S) in the sparse recovery methods is given by $S = Z/ln(\sqrt{N})$ [22], [25]. As the sparsity level decreases ($S \sim N$), the sparse recovery methods (ℓ_p-norm with $0 \leq p \leq 1$) give an equivalent of ℓ_2-norm solutions.

C. Quantitative Analysis

The Pearson correlation is used as a measurement of the degree of correlation between the target and the reconstructed image having a range of values from -1 to 1. This is a common figure of merit used in the emission tomography as well as biological imaging [25]. This measure is defined as [25]

$$PC({\mu_a}^{\mathrm{target}}, {\mu_a}^{\mathrm{recon}}) = \frac{COV({\mu_a}^{\mathrm{target}}, {\mu_a}^{\mathrm{recon}})}{\sigma({\mu_a}^{\mathrm{target}})\sigma({\mu_a}^{\mathrm{recon}})} \tag{22}$$

where ${\mu_a}^{\mathrm{target}}$ is the expected μ_a distribution and ${\mu_a}^{\mathrm{recon}}$ is the reconstructed μ_a distribution using ℓ_p-norm-based regularization ($0 \leq p \leq 2$). The COV is the covariance and σ indicates the standard deviation. This measure describes the detectability of the target.

The other metric used to measure the accuracy of the reconstruction is based on the mean value of the region of interest (ROI), the value of the ROI is proportional to the contrast recovery (the higher the mean value in the ROI the better is the contrast recovery) and higher ROI leads to better detectability of the tumor.

III. Numerical and Gelatin Phantom Experiments

A. Circular Domain Numerical Experiments (Regular Geometry)

The comparison of the performance of ℓ_p-norm ($0 \leq p \leq 2$)-based regularization methods that were discussed in this study was achieved by using a circular domain initially. The circular domain has a diameter of 86 mm which is discretized into a finite-element mesh (centred around origin), a finer one for mimicking the experimental data generation and another coarser one for the reconstruction scheme. The background optical properties of the domain was set to $\mu_a = 0.01$ mm^{-1}, and $\mu_s' = 1$ mm^{-1} having a uniform refractive index of 1.33. It had two small targets mimicking tumor region separated by a distance of 10 mm having a radius of 2.5 mm, centered around (20,7.5) and (20,$-$7.5). The tumor (target) optical properties were set to $\mu_a = 0.02$ mm^{-1}, and $\mu_s' = 1$ mm^{-1}. The target μ_a distribution is given in the Fig. 3 (top-left corner). The data-collection system had 16 fibers arranged on the boundary of the circular domain, where when one fiber acts as a source, rest act as detectors. This setup results in $16\times15 = 240$ number of measurements

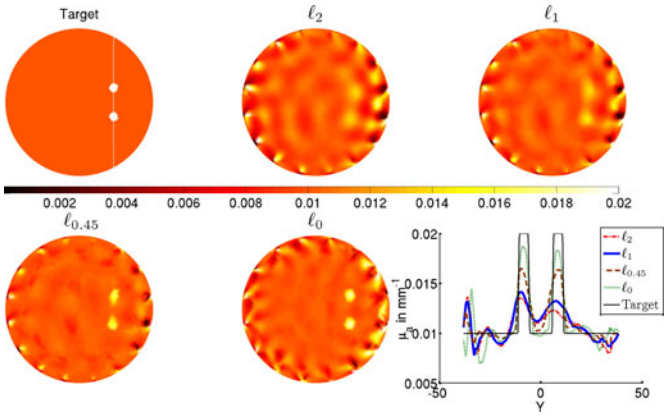

Fig. 3. Comparison of the reconstructed μ_a distribution using the ℓ_2, ℓ_1, ℓ_p, and ℓ_0 norm-based regularization scheme for the case of two small circular targets (top-left corner). The numerically generated data were corrupted with 1% normally distributed Gaussian noise. The 1-D cross section of reconstructed μ_a distribution along the solid line of target image is shown in the bottom-right corner.

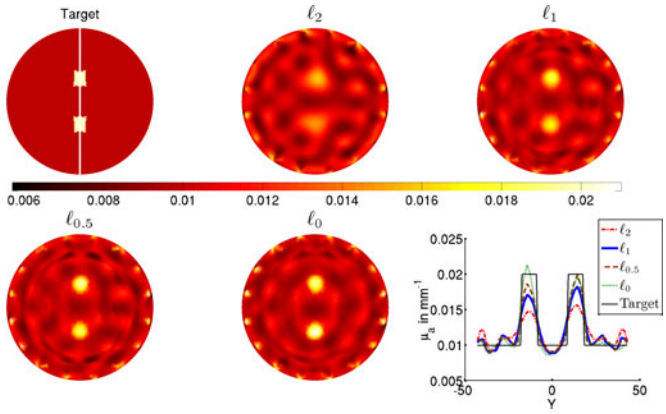

Fig. 4. Similar effort as Fig. 3, except the small targets are in rectangular in shape and are placed at the center of the imaging domain.

(M). Each source was modeled as a Gaussian source having full width at half maximum of 3 mm to mimic the experimental case [26] and is placed at one mean transport length inside the boundary. The numerical experimental data were generated using a fine mesh having 10 249 nodes (corresponding to 20 160 linear triangular elements) with addition of 1% normally distributed gaussian noise. A calibrated data were used to perform the reconstruction on a coarser mesh consisting of 1933 nodes (corresponding to 3726 linear triangular elements) [17]. The norms that were used in the reconstruction include $\ell_2, \ell_1, \ell_{0.45}$ (implemented using Algorithm 1), and smooth-ℓ_0 (implemented using Algorithm 2).

A similar effort having rectangular targets placed close to the center of imaging domain is considered to test the ability to recover sharp edges using the methods discussed in here. The rectangular absorbers are separated by 20 mm in the center of the imaging domain as shown in top-left corner of Fig. 4. The rectangles were of size 7×9 mm placed at (0,13.5) and (0,−13.5), these absorbers have the similar optical properties as of earlier case.

B. Patient Mimicking Numerical Experiments (Irregular Geometry)

To test the effectiveness of the reconstruction methods discussed in this study, a patient mimicking irregular geometry is considered with increasing data noise level. The patient mimicking mesh had an irregular boundary, the geometry was acquired in Dartmouth NIR-MRI setup [27], where the tissue morphology is captured using MRI, consisting of both fatty and fibro-glandular tissue. The background optical properties were set to same values as in circular domain case. It was assumed that there are only two regions in the tissue, tumor (target), and background (achieved by making the fibro-glandular tissue and fatty tissue into one region). Initially, a circular target mimicking the tumor with a radius of 7.5 mm is placed in the irregular imaging domain centred at (27,−7.5). The optical properties for the tumor region were kept as $\mu_a = 0.02$ mm^{-1}, $\mu_s' = 1$ mm^{-1} having 100% contrast compared to background as shown in Fig. 5. The experimental data were generated using a fine patient mesh having 4876 nodes (corresponding to 9567 linear triangular elements). This data were added with 1% and 5% normally distributed Gaussian noise. The reconstruction was performed on a coarser mesh consisting of 1969 nodes (corresponding to 3753 linear triangular elements). The data-collection strategy was similar to the previous case.

Next, a case of same geometry as earlier, but having three regions, typically observed in breast imaging, is considered. In this case, the fibro-glandular region was also irregular in nature, having optical properties as $\mu_a = 0.015$ mm^{-1}, $\mu_s' = 1$ mm^{-1}. The target and fatty tissue have taken the same values as the earlier case. The target μ_a-distribution is shown in the top-left corner of Fig. 6. In this case, the data collection and reconstruction were performed in the same fashion as the earlier case, except the data-noise level of only 1% is considered here.

C. Gelatin Phantom Experiment

The comparison of the methods that was discussed in Section II-B was also performed using an experimental gelatin phantom data, which closely mimics the typical breast composition. This phantom was prepared using a mixture of Indian ink for producing absorption effect and Titanium oxide (TiO_2) for scattering [10]. The gelatin phantom had a radius 43 mm and height of 25 mm. The layers of gelatin were fabricated by using a hardening heated gelatin solution (having a concentration of 80% of deionized water and 20% of gelatin (G2625, Sigma Inc)) successively to produce an experimentally breast mimicking phantom. The thickness of the outer layer that mimics the adipose region is 10 mm with its optical properties being $\mu_a = 0.0065$ mm^{-1} and $\mu_s' = 0.65$ mm^{-1}. The middle layer that mimics the fibro-glandular layer has a diameter of 76 mm, having the optical properties as $\mu_a = 0.01$ mm^{-1} and $\mu_s' = 1.0$ mm^{-1}. The tumor is mimicked as a cylindrical hole extending in the *Z*-direction filled with intralipid mixed with Indian ink with optical properties being $\mu_a = 0.02$ mm^{-1} and $\mu_s' = 1.2$ mm^{-1} with a radius of 8 mm and height of 24 mm. The data were collected using 785 nm light source for the validation of individual layers optical properties. The CW data were

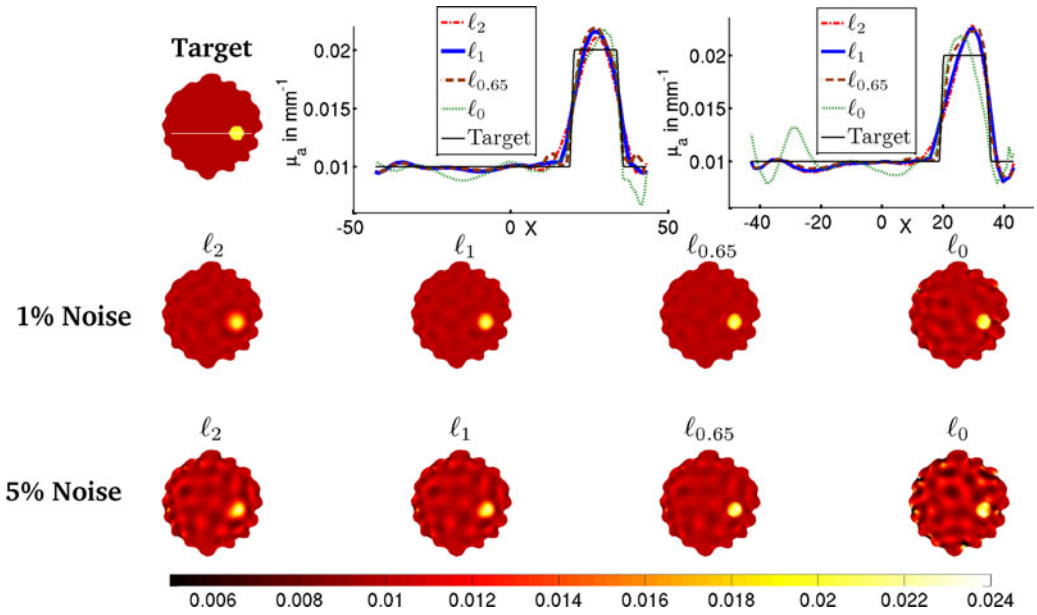

Fig. 5. Comparison of the reconstructed μ_a images obtained using ℓ_2, ℓ_1, ℓ_p, and ℓ_0 norm-based regularization scheme for an irregular geometry (mimicking typical *in vivo* case) with increasing noise level (indicated at the left hand side). The top-middle 1-D profile plot along the solid line of target image is for the data noise level of 1% and the top-right one for results obtained using 5% noisy data.

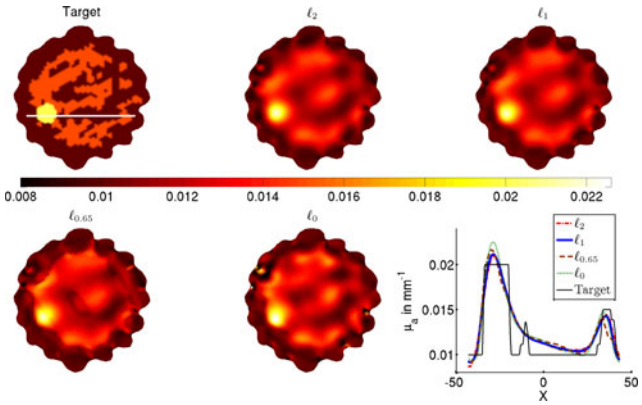

Fig. 6. Comparison of reconstructed absorption coefficient obtained for the case of irregular heterogeneous tissue, mimicking a typical breast, using ℓ_2, ℓ_1, ℓ_p, and ℓ_0 norm based regularization scheme. The data noise level is 1%. Similar to Fig. 3, the 1-D cross section of the reconstructed results are given in the bottom right corner.

collected using a single layer of fibers (at z=0 mm) leading to 240 ln A data points. The collected data were calibrated using the finite-element mesh having 1785 nodes (corresponding to 3418 linear triangular elements). All computations were carried out on a Linux work station with an Intel Xeon 5410 Dual Quad Core 2.33 GHz processor with 64 GB of RAM. The modeling of light propagation was performed using MATLAB-based open-source NIRFAST [8] and smooth-ℓ_0-norm-based Algorithm was written based on open-source code [28]. The MATLAB package was registered at Mathworks, Natick, MA, USA.

Moreover, in all cases (numerical as well as gelatin phantom), the experimental data are calibrated to remove the unwarranted biases among different channels as well as numerical errors induced by finite-element discretization [17]. The FEM-based method is a well-established numerical method for modeling light propogation, but is known to induce errors due to coarse discretization and source modeling, hence calibration is performed to provide a good initial guess [17], [29]. The data-calibration also results in initial guess (μ_a^0) [17]. The same initial guess is used for all methods for consistency. It is also important to note that the ℓ_p-norms that were considered between 0 and 1 were varied (in steps of 0.05) and then a p vs $\|y - G(\mu_{\rm arec})\|_2$ ($G(\mu_{\rm arec})$ represents the data collected using the reconstruction absorption distribution) graph was plotted, the p resulting in a minimum value of $\|y - G(\mu_{\rm arec})\|_2$ is considered as optimal p.

IV. Results

For the case of small circular targets, the reconstruction results obtained using the methods described earlier are given in Fig. 3. The 1-D cross-section profile of reconstructed μ_a distribution along the solid line of the target image of Fig. 3 is given at the bottom-right corner. Similar effort in the case of small rectangular targets is reported in Fig. 4. It is clearly evident that as the p in the ℓ_p-norm is approaching zero, the resolution as well as quantitativeness of the targets is improving, with smooth-ℓ_0-norm providing the highly desired spatial resolution as well. The circular and rectangular targets placed at the center and edge of the imaging domain were used to show the effectiveness of sparse recovery methods (in terms of spatial resolution). The rectangular targets were primarly chosen to show the capability of sparse recovery methods in reconstructing sharp edges. Note that the sensitivity of the imaging domain at the center is lower compared to the edge [30], in turn indicating that the experiments involving targets located close to the center forming the worst case scenario. This also makes the spatial resolution at the center of imaging domain comparatively lower.

The reconstruction results pertaining to the case of irregular imaging domain containing only two regions with data noise

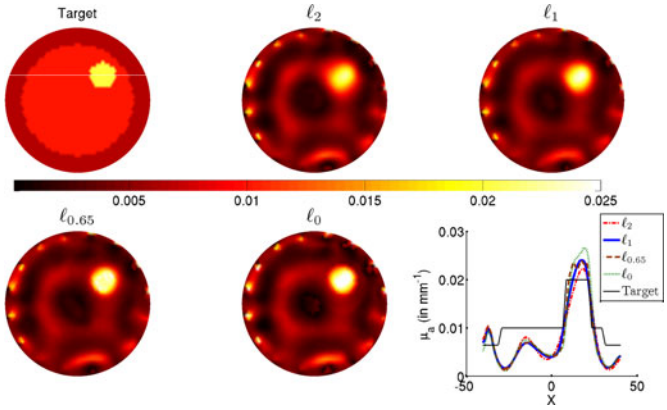

Fig. 7. Comparison of reconstructed μ_a results obtained for the case of experimental gelatin phantom, mimicking a typical breast, using ℓ_2, ℓ_1, ℓ_p, and ℓ_0 norm based regularization scheme. Similar to Fig. 3, the 1-D cross section of the reconstructed results are given in the bottom right corner.

TABLE I
SET OF RECONSTRUCTION PARAMETERS USED FOR THE RESULTS PRESENTED IN THIS STUDY

Fig.	ℓ_2	ℓ_1	ℓ_p	$Smooth-\ell_0$
Fig. 3	in_{it} = 280 d=0.1 λ = 1	in_{it} = 280 d=0.1 λ = 1	in_{it} = 270 d=0.1 λ = 1, p=0.45	λ = 1e-4 σ_{dec} = 0.6 μ_0 = 2
Fig. 4	in_{it} = 250 d=0.1 λ = 2	in_{it} = 250 d=0.1 λ = 2	in_{it} = 230 d=0.1 λ = 2, p=0.5	λ = 5e-3 σ_{dec} = 0.45 μ_0 = 2
Fig. 5 (1%)	in_{it} = 180 d=0.08 λ = 2	in_{it} = 180 d=0.08 λ = 2	in_{it} = 150 d=0.1 λ = 2, p=0.65	λ = 0.02 σ_{dec} = 0.25 μ_0 = 1.8
Fig. 5 (5%)	in_{it} = 100 d=0.1 λ = 10	in_{it} = 100 d=0.1 λ = 10	in_{it} = 100 d=0.1 λ = 10, p=0.65	λ = 0.02 σ_{dec} = 0.25 μ_0 = 1.8
Fig. 6	in_{it} = 100 d=0.07 λ = 2	in_{it} = 100 d=0.09 λ = 2	in_{it} = 110 d=0.07 λ = 2, p=0.65	λ = 0.05 σ_{dec} = 0.2 μ_0 = 0.8
Fig. 7	in_{it} = 95 d=0.09 λ = 5	in_{it} = 95 d=0.09 λ = 5	in_{it} = 90 d=0.09 λ = 5, p=0.65	λ = 0.05 σ_{dec} = 0.4 μ_0 = 1.4

levels of 1% and 5% were given in Fig. 5. Here, the 1-D line profile was given in the middle and last columns of top-row for 1% and 5% noisy data cases, respectively. For the case of heterogeneous irregular tissue containing three regions, closely mimicking typical breast, the results are presented in Fig. 6. Finally, the reconstruction results obtained for the case of experimental gelatin phantom data are given in Fig. 7. Here, ℓ_p-norm with $p = 0.65$ performed superior compared to other ones. The typical total computational time for obtaining these reconstruction results for the case of smooth-ℓ_0-norm is 20 s, and all other cases take about 45 s.

The reconstruction parameters used for performing the ℓ_0-norm and ℓ_p-norm-based reconstruction is indicated in Table I for all the experiments considered in this study. The values of the optimal p are also indicated in Table I for the nonconvex-based minimization schemes (p in ℓ_p-norm is in $0 < p < 1$). The figures of merit (Pearson Correlation and Mean μ_a in ROI) for the numerical and experimental phantom cases are indicated in Tables II and III. From these quantitative metrics, the performance of sparse recovery methods can be seen to be dependent

TABLE II
PEARSON CORRELATION OF THE RECONSTRUCTED OPTICAL PROPERTIES FOR THE RESULTS PRESENTED IN THIS STUDY

Fig.	ℓ_2	ℓ_1	ℓ_p	$Smooth-\ell_0$
Fig. 3	0.065	0.09	0.206	0.236
Fig. 4	0.348	0.484	0.525	0.537
Fig. 5 (1%)	0.864	0.913	0.931	0.944
Fig. 5 (5%)	0.731	0.783	0.868	0.651
Fig. 6	0.483	0.478	0.46	0.43
Fig. 7	0.367	0.418	0.442	0.38

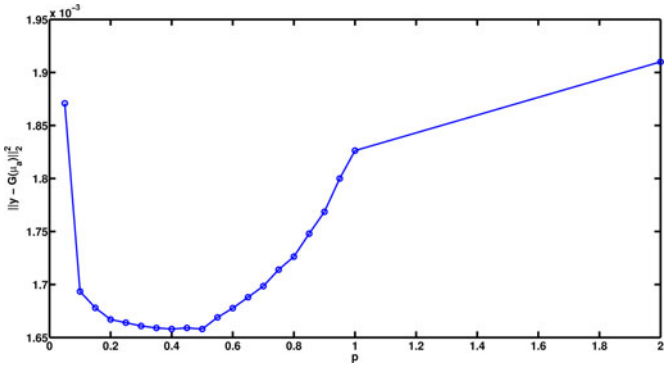

Fig. 8. Plot showing the variation of the data model misfit with experimental data (y) and reconstructed optical property distribution for a specific p in the ℓ_p-norm, corresponding to the case of Fig. 4. The p was considered in the increments of 0.05 in $0 < p < 1$.

on the data noise level as well as the expected sparseness (heterogeneity) in the solutions.

V. DISCUSSION

The sparse recovery methods have been deployed for diffuse optical tomographic image reconstruction in the past with p in the ℓ_p-norm being $0 < p \leq 1$ [11], [31]–[33]. In this study, for the first time, recently developed approximation of ℓ_0-norm [12] has been deployed, with a capability to provide more accurate sparse reconstruction results. The comparison of these sparse recovery methods has been performed systematically using both numerical and gelatin phantom experiments. Also, quantitative comparison of the reconstructed images via Pearson correlation and mean ROI values is carried through for better understanding of utilization of these sparse recovery methods.

Optimal p selection was done for the nonconvex minimization schemes. A graph indicating the procedure for selecting optimal p is shown in Fig. 8. This graph was plotted for the two small rectangular targets case (shown in Fig. 4). The graph was plotted by increasing the value of p in the intervals of 0.05 and the corresponding data-model misfit was calculated. Here, the data-model misfit is computed using the experimental data and the reconstructed absorption distribution using a particular p value. The same procedure was followed for all the other numerical and experimental phantom case.

In the case of small circular targets (see Fig. 3), where the targets span about 12 nodes in total of 1933 nodes (i.e. $S = 12$ and $N = 1933$), the minimum number of incoherent measurements required are 46 to satisfy the exact sparse recovery condition in

TABLE III
MEAN RECONSTRUCTED μ_a IN THE REGION OF INTEREST (TARGET) FOR THE THE RESULTS PRESENTED IN THIS STUDY

Fig.	ℓ_2	ℓ_1	ℓ_p	$Smooth-\ell_0$
Fig. 3	0.0121	0.0129	0.0149	0.0168
Fig. 4	0.0144	0.016	0.0169	0.0178
Fig. 5 (1%)	0.0176	0.0184	0.0189	0.0191
Fig. 5 (5%)	0.0179	0.0184	0.0196	0.0196
Fig. 6	0.018	0.0181	0.0182	0.0187
Fig. 7	0.0168	0.0183	0.0196	0.0194

compressive sensing. Recent works on measurement optimization have indicated that roughly about 40% of measurements can be considered as independent in a typical case [34]–[36]. By utilizing all measurements (240 here), the exact recovery is possible. Also as the sparseness in the solution more, the performance of ℓ_0-norm is superior as expected.

For the case of Fig. 4 ($S = 32$ and $N = 1933$), the minimum incoherent measurements required are 121, making it a weak case in terms of satisfying the exact recovery condition. The results also indicate the same, where the shape recovery is poorer compared to Fig. 3, but able to retain the quantitative accuracy. Also the expected sparseness in this case is quite lower compared to the case of Fig. 3, the deviation between $\ell_{0.5}$-norm and ℓ_0-norm is not significant, especially in Pearson correlation (see Table II).

As the sparseness level decreases, especially for heterogenous irregular tissue as in Fig. 6 ($S = 645$ and $N = 1969$), the sparse recovery methods performance are inferior compared to the traditional ℓ_2-norm case. Once again, this ascertains that sparse recovery methods may not be optimal for these scenarios. For more regular domains, still sparse recovery methods hold promise (see Fig. 7). Table III indicates the mean μ_a in the ROI, which shows that sparse recovery methods provide the best values compared to traditional ℓ_2-norm-based reconstruction method, with p being close to zero providing the best performance.

The robustness to data noise is lacking for the case of ℓ_0-norm as expected, which always demands tight bounds for the data noise levels ($< 1\%$). In these highly noisy cases, the ℓ_p-norm provides significantly better results, similar to the trend observed in Ref. [11]. These nonconvex minimization schemes (p in ℓ_p-norm being $0 < p < 1$) require much weaker incoherence conditions as compared to convex minimization schemes (p in ℓ_p-norm being $1 \leq p \leq 2$) and guarantee a successful recovery even in smaller signal to noise ratio [37]. It is important to note that this study was performed for the continuous wave case, but the discussion and trends observed in the results should hold good for both time-domain and frequency-domain case as well.

VI. CONCLUSION

The sparse recovery methods that utilize the ℓ_p-norm-based regularization schemes with $0 \leq p \leq 1$ have resulted in fast data-acquisitions in both computed tomography and magnetic resonance imaging, both of them being well-determined problems. Typical diffuse optical tomographic image reconstruction problem is severely underdetermined in nature and application of these sparse recovery methods can hold promise in improving the reconstructed image quality. More importantly, the application of smooth-ℓ_0-norm, which promotes the highest level of sparseness in the solutions is explored in this study. A systematic comparison, with decrease in the expected sparseness in the solutions, of these sparse recovery methods is performed in this study, which showed example cases where these have better utility. The reconstruction Algorithms that were developed as part of this study are available as an open-source for the enthusiastic readers/users [38].

ACKNOWLEDGMENT

The authors would like to thank the NIR imaging group at Dartmouth College for providing the necessary meshes as well as gelatin phantom data that were used in this study.

REFERENCES

[1] D. A. Boas, D. H. Brooks, E. L. Miller, C. A. DiMarzio, M. Kilmer, R. J. Gaudette, and Q. Zhang, "Imaging the body with diffuse optical tomography," *IEEE Sig. Proc. Mag.*, vol. 18, no. 6, pp. 57–75, Nov. 2001.

[2] S. Srinivasan, B. W. Pogue, S. Jiang, H. Dehghani, C. Kogel, S. Soho, J. J. Gibson, T. D. Tosteson, S. P. Poplack, and K. D. Paulsen, "Interpreting hemoglobin and water concentration, oxygen saturation and scattering measured *in vivo* by near-infrared breast tomography," *Proc. Nat. Acad. Sci. U.S.A.*, vol. 100, pp. 12349–12354, 2003.

[3] A. Gibson, J. C. Hebden, and S. R. Arridge, "Recent advances in diffuse optical tomography," *Phys. Med. Biol.*, vol. 50, pp. R1–R43, 2005.

[4] S. R. Arridge, "Optical tomography in medical imaging," *Inv. Probl.*, vol. 15, pp. R41–R93, 1999.

[5] M. Schweiger, S. R. Arridge, and D. T. Delpy, "Application of the finite element method for the forward and inverse models in optical tomography," *J. Math. Imag. Vis.*, vol. 3, pp. 263–283, 1993.

[6] A. Gibson and H. Dehghani, "Diffuse optical imaging," *Phil. Trans. R. Soc. A*, vol. 367, pp. 3055–3072, 2009.

[7] H. Dehghani, S. Srinivasan, B. W. Pogue, and A. Gibson, "Numerical modelling and image reconstruction in diffuse optical tomography," *Phil. Trans. R. Soc. A*, vol. 367, pp. 3073–3093, 2009.

[8] H. Dehghani, M. E. Eames, P. K. Yalavarthy, S. C. Davis, S. Srinivasan, C. M. Carpenter, B. W. Pogue, and K. D. Paulsen, "Near infrared optical tomography using NIRFAST: Algorithms for numerical model and image reconstruction algorithms," *Commun. Numer. Methods Eng.*, vol. 25, pp. 711–732, 2009.

[9] P. K. Yalavarthy, B. W. Pogue, H. Dehghani, and K. D. Paulsen, "Weight-matrix structured regularization provides optimal generalized least-squares estimate in diffuse optical tomography," *Med. Phys.*, vol. 34, pp. 2085–2098, 2007.

[10] R. P. K. Jagannath and P. K. Yalavarthy, "Minimal residual method provides optimal regularization parameter for diffuse optical tomography," *J. Biomed. Opt.*, vol. 17, pp. 106015-1–106015-7, 2012.

[11] S. Okawa, Y. Hoshi, and Y. Yamada, "Improvement of image quality of time-domain diffuse optical tomography with ℓ_p sparsity regularization," *Biomed. Opt. Exp.*, vol. 2, pp. 3334–3348, 2011.

[12] H. Mohimani, M. Babaie-Zadeh, and C. Jutten, "A fast approach for overcomplete sparse decomposition based on smoothed ℓ_0 norm," *IEEE Trans. Signal Process.*, vol. 57, no. 1, pp. 289–301, Jan. 2009.

[13] S. R. Arridge and M. Schweiger, "Photon-measurement density functions—Part 2: Finite-element-method calculations," *Appl. Opt.*, vol. 34, pp. 8026–8037, 1995.

[14] M. Schweiger, S. R. Arridge, M. Hiroaka, and D. T. Delpy, "The finite element model for the propagation of light in scattering media: Boundary and source conditions," *Med. Phys.*, vol. 22, pp. 1779–1792, 1995.

[15] A. H. Hielscher, A. D. Klose, and K. M. Hanson, "Gradient-based iterative image reconstruction scheme for time-resolved optical tomography," *IEEE Trans. Med. Imag.*, vol. 18, no. 3, pp. 262–271, Mar. 1999.

[16] M. Schweiger, S. R. Arridge, and I. Nissila, "Gauss-Newton method for image reconstruction in diffuse optical tomography," *Phys. Med. Biol.*, vol. 50, pp. 2365–2386, 2005.

[17] B. W. Pogue, K. D. Paulsen, H. Kaufman, and C. Abele, "Calibration of near infrared frequency-domain tissue spectroscopy for absolute absorption coefficient quantitation in neonatal head-simulating phantoms," *J. Biomed. Opt*., vol. 5, pp. 182–193, 2000.

[18] A. Majumdar and R. K. Ward, "On the choice of Compressed Sensing priors and sparsifying transforms for MR image reconstruction: An experimental study," *Signal Process. Image Commun*., vol. 27, pp. 1035–1048, 2012.

[19] (accessed on May 4, 2013). [Online]. Available: http://cnx.org/content/m32168/latest/

[20] A. Majumdar and R. K. Ward, "Under-determined non-Cartesian MR reconstruction," in *Proc. Med. Image Comput. Comput.-Assisted Intervention Conf*., 2010, pp. 513–520.

[21] R. Chartrand, "Exact reconstruction of sparse signals via non-convex minimization," *IEEE Sig. Proc. Lett*., vol. 14, no. 10, pp. 707–710, Oct. 2007.

[22] E. J. Candes, J. Romberg, and T. Tao, "Robust uncertainty principles: Exact signal reconstruction from highly incomplete frequency information," *IEEE J. Inf. Technol*., vol. 52, no. 2, pp. 489–509, Feb. 2006.

[23] A. Eftekhari, M. Babaie-Zadeh, C. Jutten, and H. A. Moghaddam, "Robust-SL0 for stable sparse representation in noisy settings," in *Proc. Int. Conf. Acoust., Speech, Signal Process*., 2009, pp. 3433–3436.

[24] M. M. Hyder and K. Mahata, "An improved smoothed ℓ^0 approximation algorithm for sparse representation," *IEEE Trans. Signal Process*., vol. 58, no. 4, pp. 2194–2205, Apr. 2010.

[25] J. Kuntz, B. Flach, R. Kueres, W. Semmler, M. Kachelrie, and S. Bartling, "Constrained reconstructions for 4-D intervention guidance," *Phys. Med. Biol*., vol. 58, pp. 3283–3300, 2013.

[26] T. O. Mcbride, B. W. Pogue, S. Jiang, U. L. Osterberg, and K. D. Paulsen, "A parallel-detection frequency-domain near-infrared tomography system for hemoglobin imaging of the breast in vivo," *Rev. Sci. Instr*., vol. 72, pp. 1817–1824, 2001.

[27] B. Brooksby, S. Jiang, C. Kogel, M. Doyley, H. Dehghani, J. B. Weaver, S. P. Poplack, B. W. Pogue, and K. D. Paulsen, "Magnetic resonance-guided near-infrared tomography of the breast," *Rev. Sci. Instrum*., vol. 75, pp. 5262–5270, 2004.

[28] (accessed on May 4, 2013). [Online]. Available: http://ee.sharif.edu/∼SLzero/

[29] S. Jiang, S. P. Poplack, K. D. Paulsen, B. W. Pogue, T. O. McBride, and M. M. Doyley, "Near-infrared breast tomography calibration with optoelastic tissue simulating phantoms," *J. Electron. Imaging*., vol. 12, pp. 613–620, 2001.

[30] P. K. Yalavarthy, H. Dehghani, B. W. Pogue, and K. D. Paulsen, "Critical computational aspects of near infrared circular tomographic imaging: Analysis of measurement number, mesh resolution and reconstruction basis," *Opt. Exp*., vol. 14, pp. 6113–6127, 2006.

[31] M. Suzen, A. Giannoula, and T. Durduran, "Compressed sensing in diffuse optical tomography," *Opt. Exp*., vol. 18, pp. 23676–23690, 2010.

[32] C. B. Shaw and P. K. Yalavarthy, "Effective contrast recovery in rapid dynamic near-infrared diffuse optical tomography using ℓ_1-norm-based linear image reconstruction method," *J. Biomed. Opt*., vol. 17, pp. 086009-1–086009-10, 2012.

[33] C. B. Shaw and P. K. Yalavarthy, "Prior image-constrained ℓ_1-norm-based reconstruction method for effective usage of structural information in diffuse optical tomography," *Opt. Lett*., vol. 37, pp. 4353–4355, 2012.

[34] L. Chen and N. G. Chen, "Optimization of source and detector configurations based on Crame–Rao lower bound analysis," *J. Biomed. Opt*., vol. 16, pp. 035001-1–035001-10, 2011.

[35] D. Karkala and P. K. Yalavarthy, "Data-resolution based optimization of the data-collection strategy for near infrared diffuse optical tomography," *Med. Phys*., vol. 39, pp. 4715–4725, 2012.

[36] J. Prakash and P. K. Yalavarthy, "Data-resolution based optimal choice of minimum required measurements for image-guided diffuse optical tomography," *Opt. Lett*., vol. 38, pp. 88–90, 2013.

[37] Q. Lyu, Z. Lin, Y. She, and C. Zhang,"A comparison of typical ℓ_p minimization algorithms," *J. Nuerocomput*., vol. 119, pp. 413–424, 2013.

[38] (accessed on Jun. 4, 2013). [Online]. Available: https://sites.google.com/site/sercmig/home/sparserecdot

Jaya Prakash received the B.Tech. degree in information technology from the Amrita School of Engineering, Bengaluru, India, in 2010, and the M.Sc. Engg.) degree in supercomputer education and research centre (SERC) from the Indian Institute of Science, Bengaluru, in November 2012, where he is currently working toward the Ph.D. degree in medical imaging. He was the coauthor of the paper chosen for ISMRM Merit Award (Summa Cum Laude) in 2012. His research interests include biomedical optical imaging, compressive sensing, GPU computing, and inverse problems in medical imaging. Mr. Prakash received the SPIE Optics and Photonics Education Scholarship and Microsoft Research Indian PhD Fellowship in 2013.

Calvin B. Shaw received the B.E. degree from the M.S. Ramaiah Institute of Technology (MSRIT), Bengaluru, India, in 2009, and the M.Sc. (Engg.) degree at Supercomputer Education and Research Centre (SERC), the Indian Institute of Science (IISc), Bengaluru, in September 2012, where he is currently working towards the Ph.D. degree in medical imaging. His research interests include biomedical optical imaging, compressive sensing, sparse recovery methods, and inverse problems in medical imaging.

Rakesh Manjappa received the B.Tech. degree in engineering physics from the Indian Institute of Technology Delhi, New Delhi, India, in 2011, and is currently working toward the Ph.D. degree from the Department of Physics, Indian Institute of Science, Bengaluru, India. His research interests include diffuse optical tomography, optical projection tomography, tissue polarimetry, and Monte Carlo modeling.

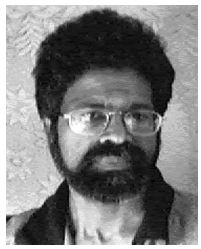

Rajan Kanhirodan received the M.Tech. and Ph.D. degrees from the Indian Institute of Science, Bangalore, India. He is an Associate Professor in the Department of Physics, Indian Institute of Science, Bangalore, India. His research interests include tomographic image reconstructions, signal and image processing, medical imaging, and embedded systems.

Phaneendra K. Yalavarthy received the M.Sc. degree in engineering from the Indian Institute of Science, Bangalore, Bengaluru, India, and the Ph.D. degree in biomedical computation from Dartmouth College, Hanover, NH, USA, in 2007. He is an Assistant Professor in Supercomputer Education and Research Centre, the Indian Institute of Science, Bangalore. His research interests include medical image computing, medical image analysis, and biomedical optics.